

Comparison of reflective band (Vis, NIR, SWIR, eSWIR) performance in daytime reduced illumination conditions

LINDSEY WILEY,^{1,*} RICHARD CAVANAUGH,¹ JOSHUA FOLLANSBEE,¹ DEREK BURRELL,¹ ROBERT GRIMMING,²  RICH PIMPINELLA,³ JEFF VOSS,³ ORGES FURXHI,⁴ AND RONALD DRIGGERS¹

¹Wyant College of Optical Sciences, University of Arizona, Tucson, Arizona 85721, USA

²CREOL, University of Central Florida, Orlando, Florida 32816, USA

³Sivananthan Laboratories, Bolingbrook, Illinois 60440, USA

⁴True Colors Infrared Imaging, Fort Collins, Colorado 80528, USA

*lindseywiley@arizona.edu

Received 5 June 2023; revised 21 August 2023; accepted 10 October 2023; posted 12 October 2023; published 24 October 2023

Daytime low-light conditions such as overcast, dawn, and dusk pose a challenge for object discrimination in the reflective bands, where the majority of illumination comes from reflected solar light. In reduced-illumination conditions, the sensor signal-to-noise ratio can suffer, inhibiting range performance for detecting, recognizing, and identifying objects of interest. This performance reduction is more apparent in the longer wavelengths where there is less solar light. Range performance models show a strong dependence on cloud type and thickness, as well as time of day across the reflective wavebands. Through an experimental and theoretical analysis of a passive sensitivity- and resolution-matched testbed, we compare Vis (0.4–0.7 μm), NIR (0.7–1 μm), SWIR (1–1.7 μm), and eSWIR (2–2.5 μm) to assess the limiting cases in which reduced illumination inhibits range performance. The time during dawn and dusk is brief yet does show significant range performance reduction for SWIR and eSWIR. Under heavy cloud cover, eSWIR suffers the most at range due to a low signal-to-noise ratio. In cases of severe reduction in illumination, we propose utilizing active illumination or the emissive component of eSWIR to improve the signal-to-noise ratio for various discrimination tasks. © 2023 Optica Publishing Group

<https://doi.org/10.1364/AO.495832>

1. INTRODUCTION

For passive imagers operating in the reflective bands, solar illumination is the primary signal-to-noise ratio (SNR) contributor [1]. On a clear day, imaging in the reflective bands is straightforward and uninhibited. However, both cloud cover and varying solar zenith angles throughout the day can greatly reduce solar irradiance. Overcast conditions as well as dawn and dusk decrease the imagery SNR and therefore range performance for passive imaging in the reflective wavebands.

Research on low-light imaging is robust, with diverse applications in astronomy, life sciences, defense, and civil service. Image intensification for low-light applications began in the early 20th century with the development of the electro-optical (EO) converter [2]. Also called image intensifying tubes, EO converters amplify electric signals generated by reflective-band photons incident on a photocathode. By amplifying the electric signal generated by scant photons, image intensifier tubes allow increased sensitivity and detection of otherwise undetectable faint objects. Several generations of image intensifiers have been developed, significantly improving the sensitivity and resolution

of imagery while decreasing costs. Despite improvements, however, intensifiers still introduce additional resolution limits on imaging systems and can introduce image artifacts, most notably adding a halo effect around bright spots. They are also susceptible to significant degradation over time [3–5].

More recently, development of low noise and high quantum efficiency in CCD and then CMOS sensors allows for low-light imaging in visible (Vis) and near infrared (NIR) wavelengths in the absence of image intensifier tubes [6–8]. The advancement of low size, weight, and power (size, weight, and power) and low-noise indium gallium arsenide (InGaAs) sensors introduces comparable low-light performance in shortwave infrared (SWIR) remote sensing [9].

Performance of sensors operating in the extended SWIR (eSWIR) band has improved with detector developments in type-II superlattice (T2SL), extending InGaAs response into longer wavelengths, and advancements in mercury cadmium telluride (MCT) focal plane array (FPA) technology [10–13]. The eSWIR band has numerous advantages over Vis, NIR, and SWIR, including high atmospheric transmission, low sky path

radiance, longer wavelengths for the reduction of scattering and absorption in the atmosphere, and better penetration through harsh environmental conditions, such as dust and smoke [14].

The simple model of the atmospheric radiative transfer of sunshine, or SMARTS, demonstrated the effect of solar zenith angle on spectral irradiance for the reflective wavebands [15]. The shorter wavelengths appear to be more affected by a change in solar zenith angle, leaving an interesting question of whether imagers operating at longer wavelengths are beneficial for low-light applications. Similarly, the use of modeling the radiation going through clouds has been studied for various remote-sensing applications, but not with specific emphasis on the performance of commercially available reflective-band sensors [16,17]. We know that clouds attenuate solar radiation, but the quantitative effect on each waveband used in daytime long-range imaging is of particular interest. Understanding the effect on imaging in low-light conditions is vital for optimal sensor selection.

The goal of this paper is to quantify the effects of reduced solar illumination in each of the reflective bands and assess object discrimination performance at range under low-light conditions using commercially available sensors. The scope of this paper is limited to non-intensified imagers because reflective-band cameras are used extensively for long-range target discrimination during the day. Passive image intensifiers are exclusively used at night under moonlight or starlight illumination conditions and can be damaged if exposed to daylight. In recent years, there have been developments to combine CCD with IR imagers for low-light applications [18]; however, the trade space of this paper focuses on solely reflective-band daytime cameras for performing an apples-to-apples comparison of the wavebands of interest.

The four wavebands analyzed in this study are Vis (0.4–0.7 μm), NIR (0.7–1 μm), SWIR (1–1.7 μm), and eSWIR (2–2.5 μm). We develop a 20° field of view (FOV) testbed to demonstrate an experimental comparison of scene imagery and target contrast in the four bands. In order to quantify the reduction of light in each band, we perform a theoretical analysis of solar illumination using the MODerate resolution atmospheric

TRANsmission (MODTRAN) model. Finally, we construct a narrow FOV testbed using the same sensors and model system performance with the reduced-illumination cases described to quantify range performance for long-range object recognition applications.

2. REDUCED SOLAR ILLUMINATION

A. Solar Zenith Angle Reduction

Solar illumination can be modeled as irradiance on the ground as a function of solar zenith angle using MODTRAN. A solar zenith angle of 0° corresponds to the sun being directly overhead, and 90° describes the sun at the horizon [19]. For the analysis in this paper, dawn and dusk assume identical conditions. Although temperature and humidity vary between dawn and dusk, the effect of solar zenith angle on irradiance is larger than the temperature or relative humidity contributions, so we neglect these effects. However, accounting for multiple scattering is necessary in the modeling of solar irradiance and drastically changes the irradiance values, especially at high solar zenith angles and shorter wavelengths. The multiple-stream DISORT discrete ordinate model is typically used for radiative transfer calculations to model multiple scattering [20]. We plot the spectral solar irradiance using the DISORT multiple scattering algorithm with eight streams for 10 different solar zenith angles, as shown in Fig. 1(a).

Figure 1(b) depicts the ratio of single scatter (no multiple scattering) to multiple scatter (DISORT) for solar zenith angles from 0° to 90° in increments of 10° using the 1976 US Standard Atmosphere model with no clouds and the rural aerosol preset. The 93rd day of the year was selected for being a seasonally temperate time of the year, not subject to large temperature and humidity variations, and is also a default in some MODTRAN models. This allows for a baseline to generalize the affect of scattering on solar irradiance on the ground. The plot shows that shorter wavelengths are more affected by multiple scattering, and therefore multiple scattering needs to be included in models of spectral solar irradiance across the reflective wavebands.

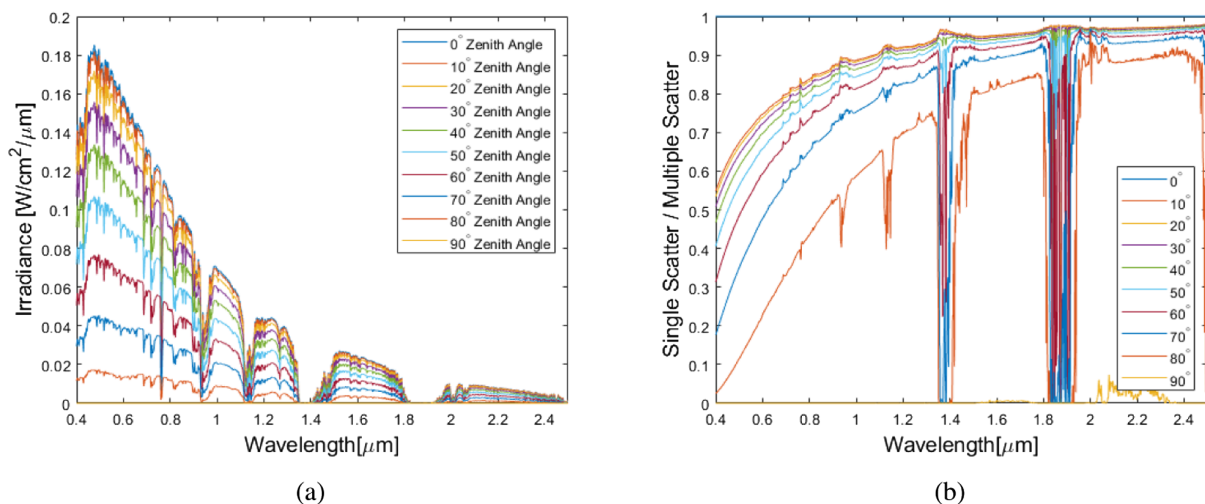


Fig. 1. (a) Spectral solar irradiance using DISORT multiple scattering; (b) ratio of single scatter to multiple scatter for direct sunlight at 10 different zenith angles.

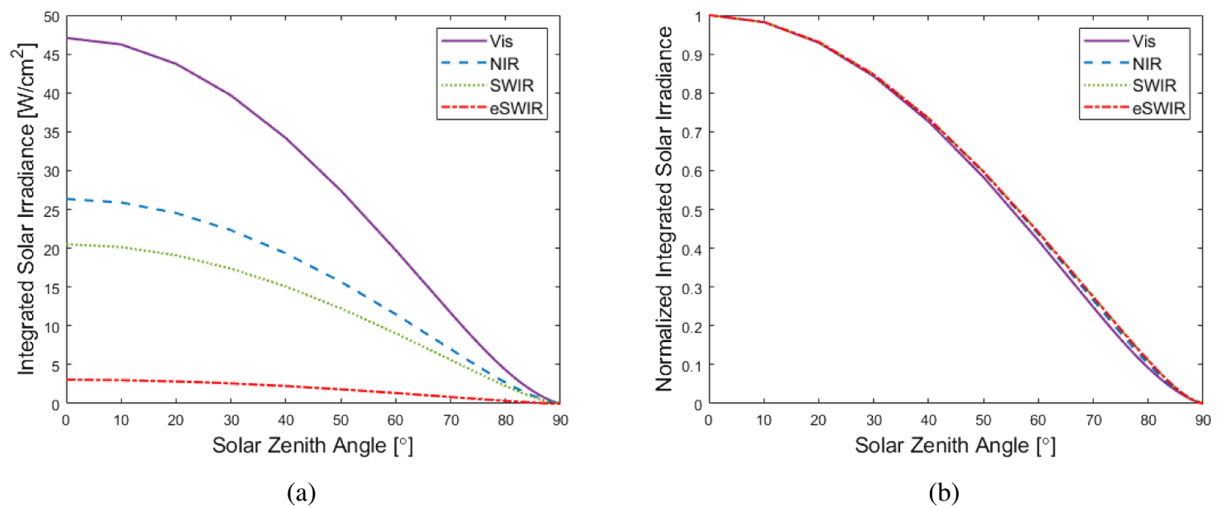


Fig. 2. (a) Absolute band-integrated irradiance and (b) normalized band-integrated irradiance for direct sunlight as a function of solar zenith angle.

Each band is affected by a reduction in irradiance as the solar zenith angle increases, equivalent to the sun approaching the horizon. This is quantified by computing the band-integrated irradiance for each waveband with a trapezoidal Riemann sum in MATLAB. Figure 2(a) displays the band-integrated irradiance from Fig. 1(a) as a function of solar zenith angle to show the reduction in light in a given waveband. When the irradiance in each band is normalized to the integrated solar irradiance of the sun directly overhead, all bands are reduced equally as a function of solar zenith angle, as seen in Fig. 2(b). Therefore, the eSWIR band, which has the least light to begin with, has the lowest solar irradiance at all solar zenith angles.

B. Cloud Cover

Another way light can be reduced during the day is by cloud cover. Clouds are typically classified by their altitude, which can roughly be categorized into three ranges: low altitude (less than 6500 ft), medium (between 6500 and 23,000 ft), and high (between 16,500 and 45,000 ft) [21]. Three of the most common clouds present in Tucson, Arizona, were selected based upon data from a 1958 repository, which reported the number of occurrences of each cloud type for a nine-year period from 1945 to 1954 [22]. These are cirrus (high altitude), altostratus (medium altitude), and cumulus (low altitude).

The solar irradiance after transmission through cloud cover was computed using MODTRAN's default cloud model for each cloud type along with the 1976 US Standard Atmosphere, rural aerosol preset, and DISORT multiple scattering with eight streams. A reasonable range of thicknesses for each cloud type was determined from a literature search, which is explained in the subsequent sections. Band-integrated irradiance values were calculated for each type of cloud from the spectral irradiance output from MODTRAN [19].

It is important to note that the cloud models in this paper were assuming uniform cloud cover to show the most debilitating cases. Cumulus and cirrus clouds can often be broken, and therefore the illumination reduction will not be as severe. The purpose of modeling uniform cloud cover is to observe the worst-case scenarios in which light reduction becomes

problematic for passive imaging in the reflective wavebands. The nuance of this paper is to demonstrate when eSWIR should and should not be chosen over other bands.

1. Cirrus Clouds

Cirrus clouds are often found very high in the atmosphere and commonly range in thickness from 0.3 to 3.8 km, with an average thickness of 1.7 km [23]. The band-integrated irradiance on the ground after transmittance through these clouds is depicted in Fig. 3(a). Each irradiance curve is normalized to a 0.5-km-thick cirrus cloud to show the reduction in illumination as a function of increasing cloud thickness in Fig. 3(b). Illumination attenuation increases for increasing wavelength, with the eSWIR band affected the most of any band. However eSWIR normalized transmission reaches about 65% over a realistic range of thicknesses for cirrus clouds, thus the light reduces by only 35% at maximum thickness.

2. Altostratus Clouds

Altostratus clouds can range in thickness from 1 to 6 km but are rarely less than 2 km thick [24,25]. Figure 4(a) displays the band-integrated irradiance as a function of cloud thickness, while Fig. 4(b) shows the irradiance normalized to a 1-km-thick altostratus cloud. Again, the illumination attenuation increases with increasing wavelength. The eSWIR band has little to no solar irradiance at any realistic thickness for altostratus clouds. Note that Fig. 4(b) omits the eSWIR band because normalizing to a value of zero is undefined.

3. Cumulus Clouds

Cumulus clouds commonly have a thickness from 1 to 3 km [24]. Figure 5(a) displays the band-integrated irradiance for these thicknesses of cumulus cloud cover, and Fig. 5(b) depicts the irradiance normalized to a 1-km-thick cumulus cloud. Similar to the altostratus cloud cover, essentially no illumination is present in the eSWIR band for the range of cumulus clouds modeled and therefore is removed from the normalization plot in Fig. 5(b).

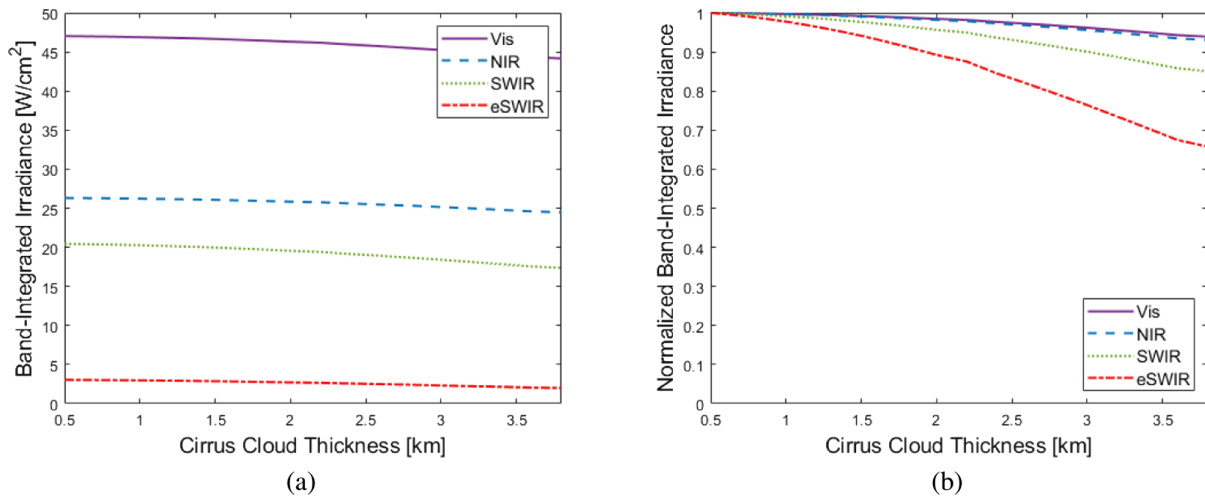


Fig. 3. (a) Absolute band-integrated irradiance and (b) normalized band-integrated irradiance for varying thicknesses of cirrus cloud cover.

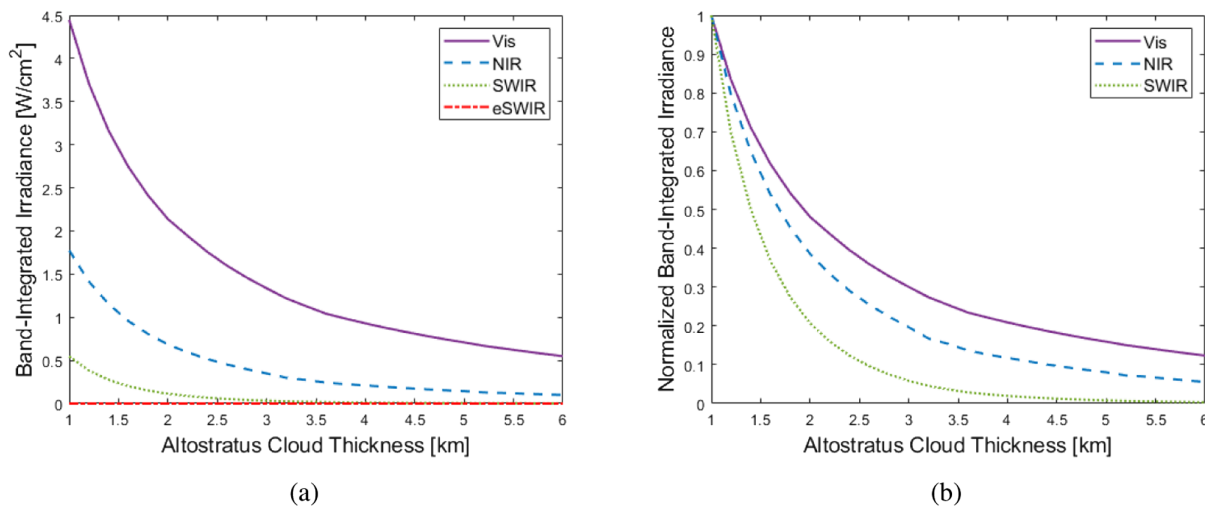


Fig. 4. (a) Absolute band-integrated irradiance and (b) normalized band-integrated irradiance for varying thicknesses of altostratus cloud cover.

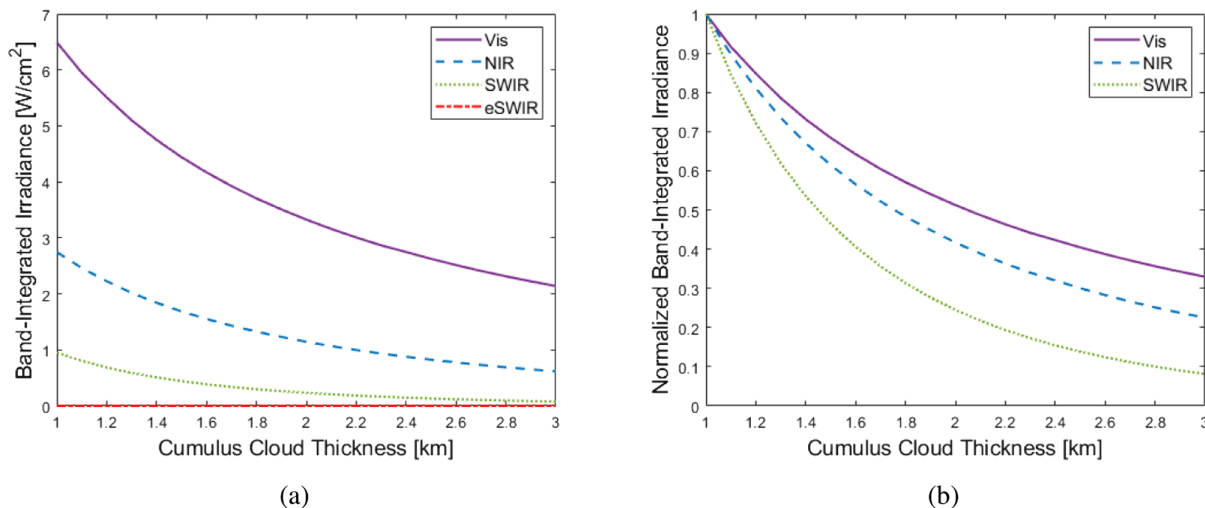


Fig. 5. (a) Absolute band-integrated irradiance and (b) normalized band-integrated irradiance for varying thicknesses of cumulus cloud cover.

Table 1. 20° FOV Testbed Specifications

Specification	Vis	NIR	SWIR	eSWIR
Spectral response (μm)	0.4–0.7	0.7–1.0	1.0–1.7	2–2.5
FPA	CMOS	CMOS	InGaAs	MCT
Format	2048 \times 2048	2048 \times 2048	640 \times 512	320 \times 256
Pitch (μm)	5.5	5.5	5	30
Horizontal FOV (deg)	18.28	18.28	22.62	21.74
Focal length (mm)	35	35	8	25

3. EXPERIMENTAL TESTBED

Four cameras were integrated into a software system to acquire simultaneous imagery. Optics for each camera were selected to image a roughly 20° FOV, with each camera mounted on a rotation stage and goniometer to allow boresighting for comparison of the same scene. The Vis and NIR cameras used were Edmund Optics EO-4010 Progressive Scan CMOS sensors with 2048 by 2048 format and 5.5- μm pitch. Low-pass and high-pass filters with a 0.7- μm cutoff were placed on the Vis and NIR cameras, respectively. With the filter, the spectral response of the Vis camera was 0.4–0.7 μm and the NIR was 0.7–1.0 μm . The SWIR camera was the Attollo Engineering Phoenix VGA with an InGaAs FPA. Its format was 640 by 512 with 5- μm pitch and spectral response of 1.0–1.7 μm . The eSWIR camera was the Photon etc. Zephyr 2.5 with an MCT FPA, 320 by 256 format and 30- μm pitch. The spectral response of the eSWIR camera with a bandpass filter was 2–2.5 μm . The specifications for the 20° FOV testbed are described in Table 1.

4. METHODS

A. Calibration

During collection of field imagery we used a black and white target to calibrate each camera. Exposure times were set by placing both an extremely low-reflectivity Vantablack [26] target and a highly reflective Spectralon [27] target in the camera frame to set the maximum available dynamic range while preventing saturation. Band-averaged reflectivities were calculated from the measured spectral reflectivity of each target. Both targets had near-Lambertian reflectivity, and during field tests, the targets were carefully placed at the same angle with respect to the sun to receive uniform illumination. The average signal level over a uniform region on each of the black and white targets was measured and matched to the band-averaged reflectivity of the corresponding target. A linear interpolation was then performed to map any given feature on an image to an “equivalent” reflectivity.

B. Dawn and Dusk

Two approaches were used to acquire imagery during dawn and dusk. The first was to hold the exposure constant and record a series of images that appear brighter or darker over time as the sun rises or sets, respectively. The second was to vary the exposure for each image acquisition time around dawn and dusk. The benefit of the constant-exposure approach was the ease of visual comparison of the images within a sequence. The drawback, however, was that images from darker scenes have a

greatly reduced dynamic range, making isolated image analysis more difficult. The variable-exposure approach aided in analysis by maximizing the dynamic range of each image but resulted in less visually intuitive image comparisons.

1. Constant Exposure

For the constant exposure data collection, the time of sunrise and sunset were recorded. The total time of daylight hours was calculated and then divided by 180° (a rough assumption) to determine the time taken for the sun to move 1°. The exposure time was set for each camera when the sun was around the 65° solar zenith angle, and then images were captured in each band from 70° every 2° until the sun reached the 90° zenith angle—the time of sunset. The exposure in the first image was selected by looking at the histogram of the scene and selecting an exposure that maximized the dynamic range for each camera.

For image analysis, both the mean and median signal levels of the same portion of the scene in each band were determined and recorded as a function of the solar zenith angle, or equivalently the time of the image. The sky was left out of the selected scene region of the image to avoid averaging over a continuous dark level.

2. Variable Exposure

The goal of the variable-exposure method was to determine the percentage of increase in exposure time needed to maximize the dynamic range of the camera for a given scene as the illumination reduced at sunset for each band. For low-light conditions, a higher noise level is sometimes seen with the higher required exposure time. The variable-exposure approach proved to be of limited usefulness for the analysis associated with this paper due to scene variations in the imagery resulting in non-uniform illumination. Similarly, comparing exposure times across different cameras with varying parameters is trivial and not straightforward.

C. Cloud Cover

In order to experimentally quantify the reduction in light due to varying levels of cloud cover, a constant exposure was set for each camera by imaging the Spectralon and Vantablack targets around mid-day under no cloud cover. An illuminance meter was placed directly above each target and oriented to align with the surface normal of each calibration target. An exposure was set for each camera by maximizing the dynamic range of the

scene containing the two targets. The illuminance and $f/\#$ of the optics were recorded for each band at the time of image acquisition. These parameters and targets remained constant, and the procedure was repeated the following day around the same time but with cloud cover. As the level of cloud cover changed, the exposure time used to capture each image was recorded. The light level was measured by calculating an average signal level over a uniform region of each target. Differential signal level was calculated by subtracting the average signal level of the black target from that of the white target. Differential signal level was then plotted as a function of illuminance for each band.

It is important to note that the illuminance is only defined in the Vis band, so it must be scaled by the photopic response of the eye in order to convert solar illuminance to irradiance for all bands. Future work includes demonstrating a way to simplify this process and generalize a conversion for the different bands, similar to the approach taken in [28].

5. RESULTS

A. Dawn and Dusk

The wide-FOV testbed was taken to Tumamoc Hill in Tucson, Arizona on 7 February 2023 to capture field imagery near dusk. The optical conditions of the experiment included 0% cloud cover, 40.7% humidity, and 16-km visibility, with an average temperature of 60°F and pressure of 30.16 inHg at the time of collection [29,30]. The procedure described in Section 4.B.1 was followed, setting the integration time for each band using the available contrast in the scene. Once the exposure was set prior to the 70° solar zenith angle, it was held constant for the remainder of the data collection. Imagery was collected in increments of 2° but is displayed in increments of 4° for better visual comparison in Fig. 6.

The imagery in Fig. 6 was analyzed by the methodology described in Section 4.B.1, and the median gray level of the scene excluding the sky was taken for each image. Figure 7(a)

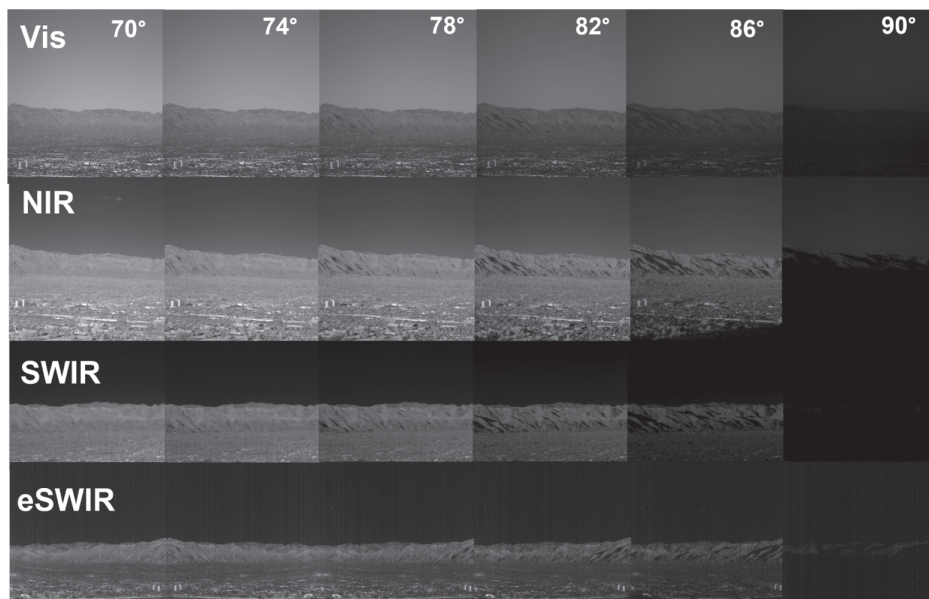


Fig. 6. Progression of wide FOV imagery near dusk with fixed exposure in each band.

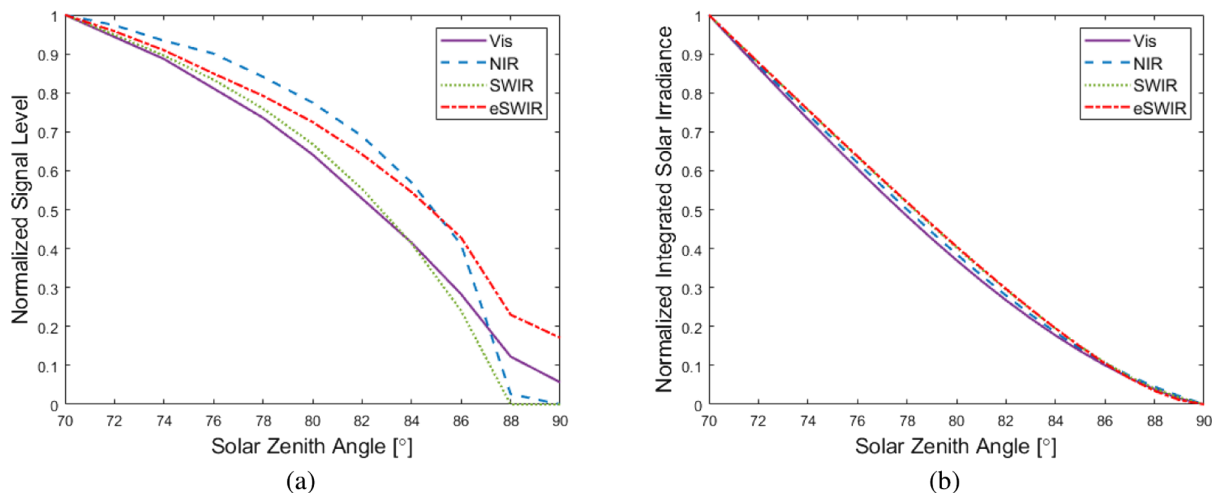


Fig. 7. (a) Median scene gray level from experimental imagery; (b) modeled solar irradiance normalized to 70° solar zenith angle.

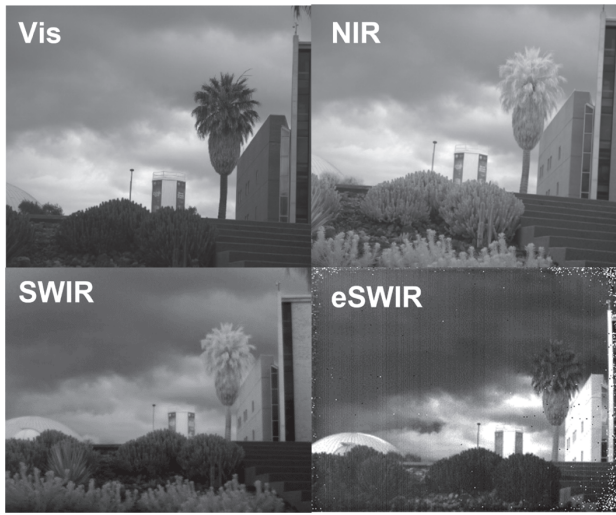


Fig. 8. Wide FOV testbed overcast imagery.

portrays the experimental data while Fig. 7(b) shows the modeled MODTRAN solar irradiance reduction for each band. Both plots are normalized to the 70° solar zenith angle for each band. The inflection difference between the measured and calculated values could be caused by a nonlinear signal intensity transfer function (SITF) or, more likely, atmospheric differences between modeled and real conditions.

B. Cloud Cover

Figure 8 shows imagery from a heavy cloud cover day in Tucson on 21 February 2023. The optical conditions at the time of the collection included 86.8% cloud cover at around 7000 ft of elevation, 68.3% humidity, 15.8-km visibility, at 60°F and 29.73 in Hg [29,30]. The optics of all four sensors were matched at roughly $f/2.6$. The eSWIR exposure was set to 25 ms, while the Vis was 0.525 ms (roughly a factor of 50 difference between the two). Even with the longer exposure time, the eSWIR band has substantially lower SNR, with fixed-pattern and read noise beginning to appear in cases of reduced illumination.

6. APPLICATION

In order to perform object discrimination at long ranges, a narrow-FOV testbed was designed, matching each of the sensors from the 20° FOV testbed with longer-focal-length telescopes with roughly the same $f/\#$ and instantaneous field of view (IFOV). Table 2 summarizes the corresponding specifications of the narrow-FOV testbed for modeling sensor system range performance and collecting field imagery. Note that the large pixel size of the eSWIR camera required an inconveniently long-focal-length optic compared to the other bands.

We perform range calculations with the US Army's Night Vision Integrated Performance Model (NV-IPM) using the sensor parameters of the narrow-FOV testbed. NV-IPM takes inputs of over 100 parameters including illumination, target and background, atmospheric, optics, detector, electronics, and display inputs. The model uses the system modulation transfer function (MTF) and the contrast threshold function (CTF) of the naked eye to calculate the system CTF:

Table 2. Narrow-FOV Testbed Specifications

Specification	Vis	NIR	SWIR	eSWIR
Aperture diameter (mm)	76	76	76	406
Focal length (mm)	300	300	300	1800
Horizontal FOV (deg)	2.15	2.15	0.61	0.31
IFOV (mrads)	0.01833	0.01833	0.01667	0.01667
$f/\#$	$f/3.9$	$f/3.9$	$f/3.9$	$f/4.4$
$F\lambda/d$	0.39	0.6027	1.053	0.33

$$C_{\text{sys}}(\xi) = \frac{\text{CTF}(\xi)}{\text{MTF}(\xi)} \left(1 + \frac{\alpha^2 \sigma^2}{L^2} \right)^{1/2}, \quad (1)$$

where α is a calibration constant that relates noise with luminance, σ is a measure of noise sensed by the eye, and L is the display luminance, as described in [31]. NV-IPM then calculates the target task performance (TTP) metric, which roughly corresponds to an integrated number of cycles on target and combines both sensitivity and resolution into a single measure:

$$\text{TTP} = \int_{\xi_{\text{cut-on}}}^{\xi_{\text{cut-off}}} \left(\frac{C_{\text{TGT}}}{\text{CTF}_{\text{sys}}(\xi)} \right)^{1/2} d\xi. \quad (2)$$

The number of cycles on target is compared to V50, an empirical measure of task difficulty, to perform various levels of discrimination (detection, recognition, and identification). A given task is performed with 50% probability of success when the TTP value equals the V50. The ratio of number of cycles on target to V50 becomes the input to the target transfer probability function (TTPF), or

$$V(R) = \text{TTP} \frac{\sqrt{A_{\text{tgt}}}}{R}, \quad (3)$$

where A_{tgt} is the area of the target, and R is the range to the target, which can be computed for a specified number of ranges. The model outputs a probability curve as a function of range, given by

$$P(R) = \frac{\left(\frac{V(R)}{V_{50}} \right)^E}{1 + \left(\frac{V(R)}{V_{50}} \right)^E}, \quad (4)$$

where the exponent E can vary, but for most applications is 1.5 [1]. The probability curves can then be compared to assess range performance for a given scenario where all other inputs are matched. All of the models in this section use a V50 of 7.5, corresponding to the task of recognition [31,32].

We select a 3.11-m characteristic dimension target with spectral reflectivity as shown in Fig. 9, against a background with known spectral reflectivity. The target and background reflectivities are chosen such that the band-averaged differential reflectivity, $\rho_{\text{tgt}} - \rho_{\text{bkg}}$, is fairly consistent across all four bands. This allows for isolation of illumination and atmospheric transmission as the primary components of interest for determining range performance. The band-averaged reflectivities of both the target and background are computed for each waveband before taking their difference. The relevant values are displayed in Table 3.

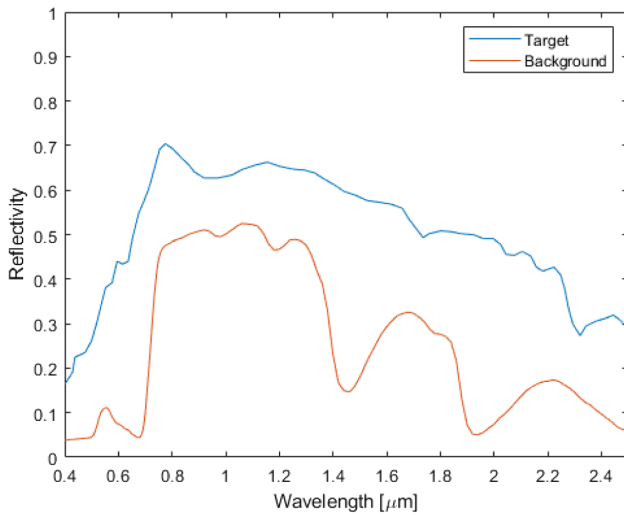


Fig. 9. Spectral reflectivity for selected target and background in NV-IPM models.

Table 3. Target and Background Band-Averaged Reflectivities

	Vis	NIR	SWIR	eSWIR
Target	0.37	0.66	0.61	0.37
Background	0.06	0.4	0.37	0.12
Differential	0.31	0.26	0.24	0.25

A. Range Reduction with Increasing Solar Zenith Angle

Figure 10(a) shows the modeled range performance using NV-IPM for solar zenith angles from 0° to 90° for the target and background specified with the 1976 US Standard Atmosphere and direct sunlight illumination from MODTRAN computed every 10°. The output is the range where the probability of recognition equals 80% for a V50 value of 7.5. Figure 10(b) depicts the same scenario, specifically looking at solar zenith angles from 70° to 90°, using a 1° zenith angle sample spacing to expand the effect of dawn and dusk. eSWIR has the highest range performance for all solar zenith angles up until 82°. Both Vis and NIR perform better at low sun angles because they do

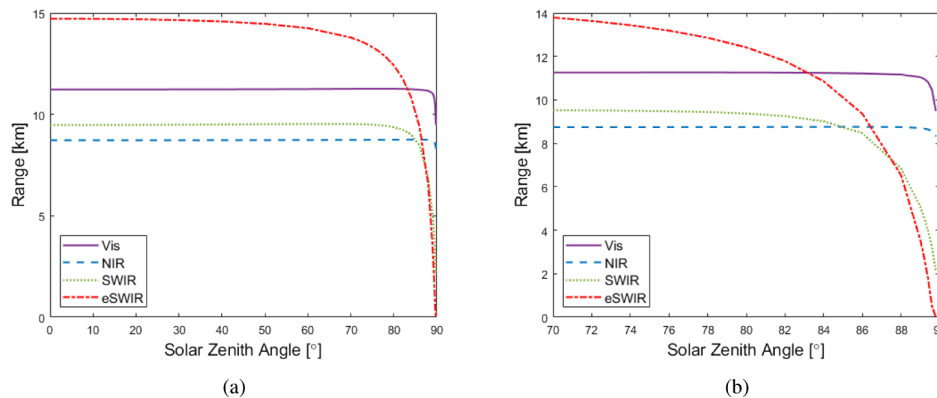


Fig. 10. Range for 80% probability of recognition as a function of solar zenith angle using NVIPM for (a) 0° to 90° and (b) 70° to 90° solar zenith angles.

not experience a decrease in range for $P(\text{rec}) = 0.8$ until right around 90°.

B. Cloud Cover

Figure 11 displays the modeled range performance using NV-IPM for the common range of thicknesses for each type of cloud: cirrus, altostratus, and cumulus. Cirrus cloud cover does not appear to have an effect on range performance for any of the bands, as seen in Fig. 11(a). Altostratus and cumulus clouds degrade eSWIR performance entirely, and SWIR performance reduces with increasing cloud thickness. The Vis and NIR bands appear unaffected in these two modeled cases.

7. DISCUSSION

Of the reflective-band irradiance for the sun directly overhead with no clouds, the Vis, NIR, SWIR, and eSWIR bands provide 0.0328, 0.0225, 0.0194, and 0.003 W/cm², respectively [14]. Considering the shortest and longest wavelength bands, eSWIR irradiance is about one-tenth that of the Vis band. However, given that Vis photons are centered at roughly 0.5 μm, and eSWIR is roughly 2.25 μm in wavelength, there are around four times the number of photons in the eSWIR for the same energy flux [J/s or W]. Multiplying these two factors yields about 2.5 times fewer photons in the eSWIR than in Vis, so even with comparable quantum efficiencies, eSWIR sensors will likely have lower SNR.

Of the two cases considered (dawn/dusk and cloud cover), the solar zenith angle has less impact on the eSWIR performance overall. With multiple scattering, the reduction in light with zenith angle appears to degrade the light level similarly across all bands. This was shown through both theoretical MODTRAN analysis and measured camera outputs. The difference in the measured versus the calculated reductions is likely due to atmospheric conditions that differ from the 1976 US Standard Atmosphere. However, both the theoretical and experimental analyses agreed with the illumination reducing similarly as a function of zenith angle in all four bands.

The plots depicting the impact of solar zenith angle on range performance show that eSWIR performance starts reducing around 70° [see Fig. 10(a)]. Significant reduction (over a third) occurs around 84°. Averaging the shortest and longest day of the

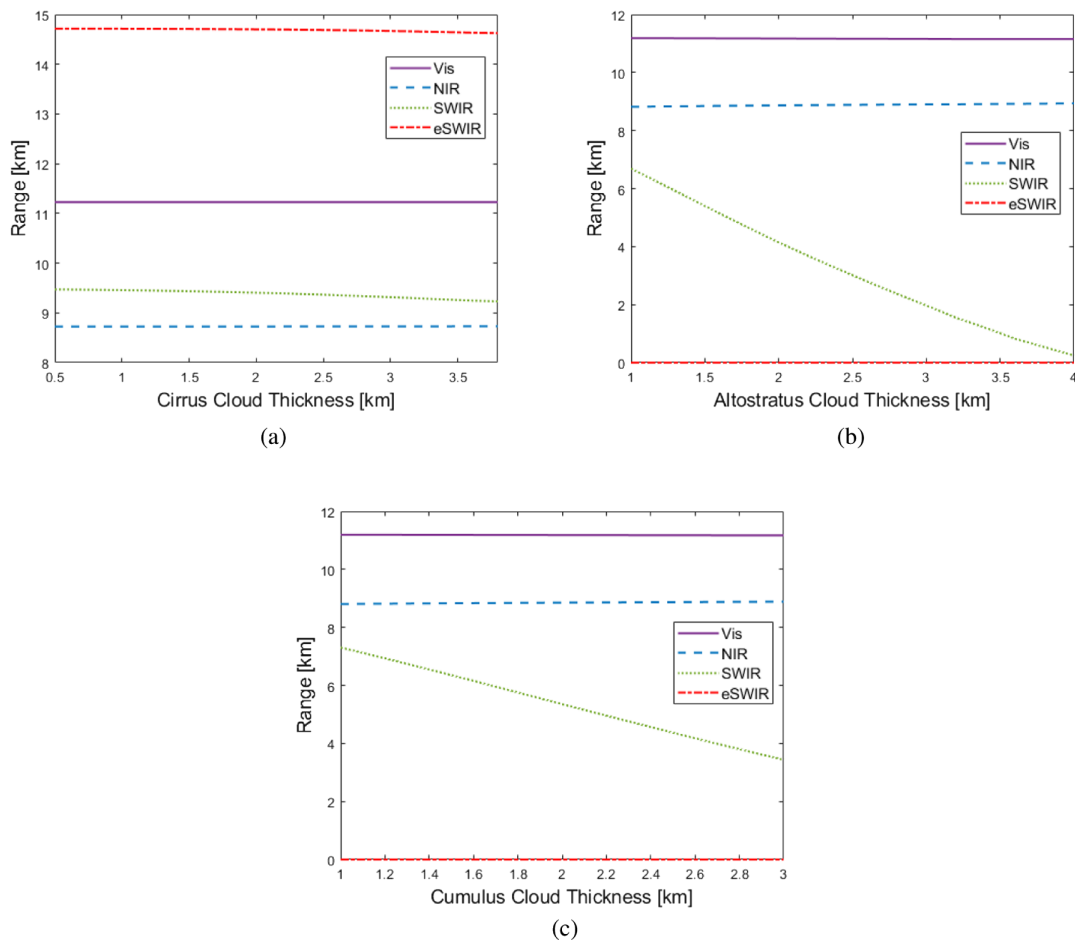


Fig. 11. Range for probability of recognition equal to 80% as a function of cloud thickness using NVIPM for narrow-FOV testbed. (a) Cirrus, (b) altostratus, and (c) cumulus.

year for Tucson, Arizona, from a weather database, each degree accounts for roughly 4 min [33]. The six degrees from 84° to the horizon therefore account for 24 min where eSWIR suffers significantly. Including both dawn and dusk, the total time is 48 min of the day. For SWIR, significant reduction occurs at around 88° , for a total loss of 16 min in the day. For Vis and NIR, the loss is negligible.

Clouds cause a more debilitating reduction in illumination for eSWIR. Figures 3–5 show the reduction in illumination with cloud cover as a function of thickness. Though the uniform cloud thickness assumption is not accurate in all scenarios, the integrated cloud irradiance provides useful trends that suggest severe degradation in eSWIR performance under overcast conditions, i.e., full cloud cover. While the effect of cirrus clouds is minimal, denser clouds such as altostratus and cumulus prevent usable eSWIR range performance and can significantly degrade SWIR performance. There is reason to believe that the extinction coefficients associated with the cloud size distributions in MODTRAN for altostratus and cumulus are not representative of real observation and therefore could be inaccurate. Figure 12 shows an eSWIR image during heavy cloud cover. Under these conditions, the integration time is maximized and the emitted flux starts competing with the reflected flux, which can be useful



Fig. 12. eSWIR image on overcast day.

for detection of hot objects, but less so for terrestrial temperature scenes.

A. Emissive Component of eSWIR

The eSWIR band also has a weak thermal component, which is normally insignificant compared to the much stronger reflected

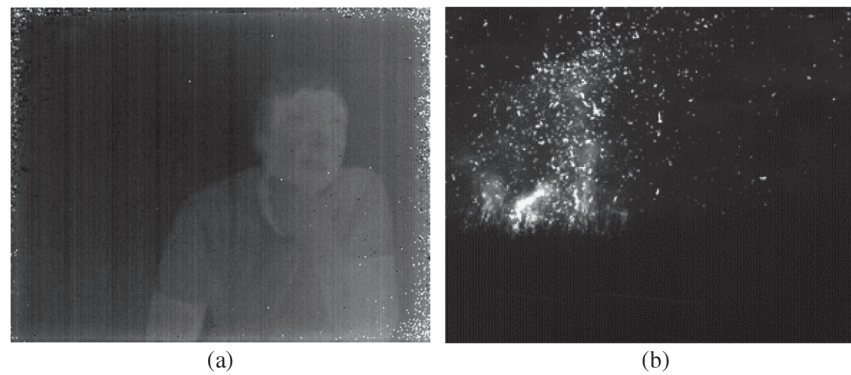


Fig. 13. Emissive signal apparent in eSWIR image of (a) human subject and (b) controlled fire.

signal. The image in Fig. 13(a) was taken indoors with no illumination and a long integration time on the order of 30 ms. The image demonstrates thermal emission from body heat that can be seen when the integration time is increased. Similarly, Fig. 13(b) was taken at a controlled burn for wildfire prevention in Tucson, Arizona, during the day, where heat signatures of the fire were apparent. Additional work by our group will explore the eSWIR band for firefighting; the band is well suited for this due to its better transmission through smoke and ability to locate hot spots of the fire. eSWIR sensors have the unique feature of capturing both reflective and emissive signals and therefore may be advantageous in a variety of applications.

8. CONCLUSIONS

The results of this research indicate that the range performance of passive imaging in the reflective bands is inhibited by cloud cover and dawn and dusk illumination more noticeably in the longer wavelengths. However, range performance does not scale directly with reduction in illumination. Specifically, as the solar zenith angle changes under clear skies, each band appears to reduce evenly, yet only SWIR and eSWIR range performance is affected due to the lower intrinsic illumination levels at these bands. The Vis and NIR bands still have enough light until higher solar zenith angles (around dawn and dusk) to achieve a high SNR and high probability of recognition. Cloud cover causes reduction in illumination in all bands, but SWIR and eSWIR performances are most affected. The amount of reduction is highly dependent upon type of cloud, its extinction coefficient, and thickness.

The methodology in this paper can be extrapolated for a wide range of scenarios if the correct atmosphere, aerosol, and desired conditions are modeled. Future work aims at matching modeled atmospheric conditions to experimental results.

While the eSWIR band usually outperforms other reflective bands for long-range object discrimination applications due to its high atmospheric transmission and low sky path radiance, it is also the most negatively affected by low-light conditions. The period of significantly degraded performance during dawn and dusk is brief and thus probably of little concern, but the NV-IPM models suggest a need for more experimental data on eSWIR performance under cloud cover, extending to broken clouds. The emissive component of eSWIR has potential to

be exploited, and active eSWIR can also provide a solution for object discrimination in cases of severely reduced illumination.

Funding. Sivananthan Laboratories Inc.

Acknowledgment. The authors acknowledge University of Arizona undergraduate research assistants Shane Jordan and Jamie Ledbetter for their assistance throughout the ongoing research study. We also thank the University of Arizona Desert Laboratory at Tumamoc Hill for providing access to a data collection spot used in this study.

Disclosures. The authors declare no conflicts of interest.

Data availability. Data underlying the results presented in this paper are not publicly available at this time but may be obtained from the authors upon reasonable request.

REFERENCES

1. R. G. Driggers, M. H. Friedman, and J. M. Nichols, *Introduction to Infrared and Electro-Optical Systems* (Artech House, 2012).
2. G. Holst, J. De Boer, M. Teves, and C. Veenemans, "An apparatus for the transformation of light of long wavelength into light of short wavelength," *Physica* **1**, 297–305 (1934).
3. E. Richards, "Fundamental limitations in the low light-level performance of direct-view image-intensifier systems," *Infrared Phys.* **8**, 101–115 (1968).
4. S. Jeffers, "Image intensifier systems and their applications to astronomy," *Opt. Eng.* **11**, 48–53 (1972).
5. D. Cui, F. L. Ren, J. Shi, Y. Shi, H. W. Qian, and B. Chang, "Test and analysis of the halo in low-light-level image intensifiers," *Chin. Opt. Lett.* **10**, S20201 (2012).
6. P. Jerram, P. J. Pool, R. Bell, D. J. Burt, S. Bowring, S. Spencer, M. Hazelwood, I. Moody, N. Catlett, and P. S. Heyes, "The LLCCD: low-light imaging without the need for an intensifier," *Proc. SPIE* **4306**, 178–186 (2001).
7. B. Fowler, C. Liu, S. Mims, J. Balicki, W. Li, H. Do, and P. Vu, "Low-light-level CMOS image sensor for digitally fused night vision systems," *Proc. SPIE* **7298**, 72981D (2009).
8. F. Wang, M. Dai, Q. Sun, and L. Ai, "Design and implementation of CMOS-based low-light level night-vision imaging system," *Proc. SPIE* **11763**, 117635O (2021).
9. R. Fraenkel, E. Berkowicz, L. Bikov, R. Elishkov, A. Giladi, I. Hirsh, E. Ilan, C. Jakobson, P. Kondrashov, E. Louzon, I. Nevo, I. Pivnik, A. Tuito, and S. Vasserman, "Development of low-swap and low-noise ingaas detectors," *Proc. SPIE* **10177**, 11–18 (2017).
10. D. Z.-Y. Ting, A. Soibel, L. Höglund, J. Nguyen, C. J. Hill, A. Khoshakhlagh, and S. D. Gunapala, "Chapter 1 - Type-II superlattice infrared detectors," in *Advances in Infrared Photodetectors*, , S. D. Gunapala, D. R. Rhiger, and C. Jagadish, eds., *Semiconductors and Semimetals* (Elsevier, 2011), Vol. **84**, pp. 1–57.

11. G. W. Wicks, T. D. Golding, M. Jain, G. R. Savich, D. E. Sidor, X. Du, M. C. Debnath, T. D. Mishima, and M. B. Santos, "Extended-shortwave infrared unipolar barrier detectors," *Proc. SPIE* **9370**, 937023 (2015).
12. N. D. Akhavan, G. A. Umana-Membreno, J. A. R. Gu, and L. Faraone, "Design principles for high QE HgCdTe infrared photodetectors for eSWIR applications," *J. Electron. Mater.* **51**, 4742–4751 (2022).
13. G. A. Tidhar and R. Segal, "New applications with a SWIR imager employing extended wavelengths," *Proc. SPIE* **8012**, 801207 (2011).
14. L. Wiley, J. Follansbee, P. Leslie, O. Furxhi, R. Pimpinella, D. Brady, and R. Driggers, "Target discrimination in the extended shortwave infrared band (2 to 2.5 μm) compared with visible, near-infrared, and SWIR in degraded visual environments," *Opt. Eng.* **61**, 113103 (2022).
15. G. Xiao, K. Guo, W. Xu, M. Ni, Z. Luo, and K. Cen, "An improved method of Lambertian CCD-camera radiation flux measurement based on smarts (simple model of the atmospheric radiative transfer of sunshine) to reduce spectral errors," *Energy* **67**, 74–80 (2014).
16. R. Guzzi, O. Vittori, and C. Tomasi, "Sun spectra through optically thin clouds," *J. Atmos. Sci.* **31**, 251–254 (1974).
17. A. Orsini, C. Tomasi, F. Calzolari, M. Nardino, A. Cacciari, and T. Georgiadis, "Cloud cover classification through simultaneous ground-based measurements of solar and infrared radiation," *Atmos. Res.* **61**, 251–275 (2002).
18. T. Vogelsong, J. Tower, T. Senko, P. Levine, J. Janesick, J. Zhu, D. Zhang, G. van der Wal, and M. Piacentino, "Low-light NV-CMOS image sensors for day/night imaging," *Proc. SPIE* **8713**, 87130F (2013).
19. "The MODTRAN 2/3 report and LOWTRAN 7 model," 1996.
20. K. Stamnes, S.-C. Tsay, K. Jayaweera, and W. Wiscombe, "Numerically stable algorithm for discrete-ordinate-method radiative transfer in multiple scattering and emitting layered media," *Appl. Opt.* **27**, 2502–2509 (1988).
21. "National oceanic and atmospheric administration the four core types of clouds," 2023.
22. R. B. DesJardins, "The distribution of clouds at Tucson, Arizona, with respect to type, amount, and time of observation," (1958).
23. H. Bui, D. Trung, N. Tuan, D. Thang, and B. Nguyen, "Monitoring cirrus cloud and tropopause height over Hanoi using a compact lidar system," *Commun. Phys.* **22**, 357 (2012).
24. A. Rangno, "Clouds | classification," in *Encyclopedia of Atmospheric Sciences*, J. R. Holton, ed. (Academic, 2003), pp. 467–475.
25. "International cloud atlas," (2017).
26. "Vantablack VBx automotive datasheet," Surrey Nanosystems Ltd, 2023.
27. "Spectralon diffuse reflectance targets datasheet," Labsphere, 2023.
28. A. Richards, M. Hübner, and M. Vollmer, "Measurements of SWIR backgrounds using the SWUX unit of measure," *Proc. SPIE* **10625**, 106250P (2018).
29. <https://visualcrossing.com>, 2023.
30. <https://weatherspark.com>, 2023.
31. R. H. Vollmerhausen, E. L. Jacobs, and R. G. Driggers, "New metric for predicting target acquisition performance," *Proc. SPIE* **5076**, 28–40 (2003).
32. "Night vision integrated performance model(NV-IPM) users guide, recommended V50 table and help file computer software," 2019.
33. <https://timeanddate.com>, 2023.